

Dynamic particle trapping, release, and sorting by microvortices on a substrate

Shui-Jin Liu, Hsien-Hung Wei, and Shyh-Hong Hwang*

Department of Chemical Engineering, National Cheng Kung University, Tainan 70101, Taiwan, Republic of China

Hsueh-Chia Chang

Department of Chemical and Biomolecular Engineering, University of Notre Dame, Notre Dame, Indiana 46556, USA

(Received 22 February 2010; published 16 August 2010)

This paper examines particle trapping and release in confined microvortex flows, including those near a solid surface due to variations in the electrokinetic slip velocity and those at a liquid-gas interface due to an external momentum source. We derive a general analytical solution for a two-dimensional microvortex flow within a semicircular cap. We also use a bifurcation theory on the kinetic equation of particles under various velocity and force fields to delineate the conditions for a vortex trap, a point trap, a limit cycle trap, and the selective sorting of the particles into different traps. In the presence of only divergence-free forces on suspended particles, we find that two parameters, such as those related to Stokes drag, gravity, and flow vorticity, are sufficient to classify all the trap topologies for a given slip velocity distribution. We also show that nondivergence-free forces such as nonuniform repulsion or attraction can capture suspended particles in one trap and selectively sort a binary suspension into different traps.

DOI: [10.1103/PhysRevE.82.026308](https://doi.org/10.1103/PhysRevE.82.026308)

PACS number(s): 47.32.C-, 72.20.Jv, 47.15.G-, 87.80.Fe

I. INTRODUCTION

The advent of microfluidic technology has stimulated growing demands in precisely controlling and manipulating micro-/nanocolloids, biological cells, and even molecules in the liquid samples. Due to the low diffusivity of such particles, Brownian transport to a localized sensor location often requires unacceptably long time—the current DNA microarray requires hour-long diffusive time for the target to the probe pixels. There is hence considerable interest in using flow to enhance the transport of the particles and molecules to the probes. For surface assays over an entire surface, flow can quickly replenish docked target molecules to reduce the diffusion length of undocked ones to the surface probes [1].

However, for more localized sensors, particularly optical ones, the transport of the particles needs to be focused toward a localized region where the sensor is located. The incompressibility of the flow field stipulates that a purely convective particle transport cannot cause this focusing. The strategy is then to combine a microvortex circulation with another force on the particles (like electrostatic attraction from a point electrode, dielectrophoresis, thermal diffusive force due to reactive depletion or gravity), such that trapping at a localized position can occur [2–4]. The convective microvortex flow allows long-range convection toward the stagnation point of the vortex flow where a short-range force then traps the particles at that location. As the convective flow effect is typically much larger than the force effect (high Peclet number), this multiscale trap is hence much more rapid and long range than those relying just on Brownian transport or short-range forces. It was also realized that, quite curiously, trapping can only occur at a converging stagnation point of the vortex flow field, as the short-range force

on particles is unidirectional and can hence only reverse the direction of the outgoing convective particle transport at a converging stagnation point.

Several such multiscale particle and molecular traps with converging stagnation points were reported recently. Hou *et al.* [5] used an ionic wind point momentum source to generate a spiral flow (with a secondary vortex flow) and trap bacteria by gravity at the stagnation point of the spiral flow for Raman spectroscopy by a laser beam 10-microns in dimension. Concentration by five to six orders of magnitude can be achieved within 15 min for an mm-sized reservoir, about three to four orders of magnitude faster than relying on diffusive sampling. A more detailed experimental scrutiny of the ionic-wind generated particle trap has revealed that the point particle trap can sometimes evolve into a vortex trap, where the particles are confined to a closed streamline or the region within it, when the force on a particle is low and can produce no trapping under other conditions [6].

One means of generating microvortices is by electro-osmotic flow (EOF) over a surface with nonuniform Zeta potentials either by functionalization or induced-charge electro-osmosis (ICEO) [7–11]. Zeta potential is electric potential on the slipping plane in the interfacial double layer versus the fluid bulk. Vortex flow can also arise from AC electro-osmosis (ACEO), where flow is generated by the action of an AC electric field on its own induced diffuse charges near a polarizable surface [12–14]. In both ICEO and ACEO, the electrokinetic slip velocity on a surface is nonlinear with respect to the applied field and varies with position, thus causing vortex flows of diverse features.

Particle trapping by microvortices generated by ICEO with a dc field was first reported by Thamida and Chang [7]. However, the most convenient means of generating microvortices for trapping particles was by ACEO. Since the pioneering work of Holmes and Morgan [15], this ACEO vortex trapping strategy has been extended to concentrating bacteria [2,16] and DNA [17,18]. DNA trapping by ACEO was shown to have a factor of several tens in concentration en-

*Author to whom correspondence should be addressed; shhwang@mail.ncku.edu.tw

richment within just a few seconds, allowing fast sample detection with enhanced fluorescent intensity [18]. However, Hou and Chang [19] have recently found that, like the interfacial vortex traps of Yeo *et al.* [6], such ACEO microvortex point traps often transform into a cylinder or ring trap, where the trapped particles are confined not to a point but to either the surface of a rotating cylinder or ring.

The dynamics of small particles in vortex flows also play an important role in nature and in technological applications. Maxey and Riley [20] established a kinetic equation for describing the motion of small spherical particles in an unsteady nonuniform flow field. Rubin *et al.* [21] studied the settling of heavy (aerosol) particles in a two-dimensional cellular flow field. They showed that arbitrarily small inertial effects can induce almost all particles to settle under gravity and that inertial particles are attracted to globally stable periodic paths. Druzhinin *et al.* [22] examined the regular and chaotic advection of small particles driven by pressure gradient, inertial and added-mass forces in a cellular or axisymmetric flow in the inviscid limit. Angilella [23] analyzed chaotic particle settling and trapping in the same two-dimensional flows submitted to a weak time-periodic perturbation. The effects of particle inertia and flow unsteadiness were investigated. The behavior of heavy particles in turbulent flows can be revealed by studying their motion in a periodic Stuart vortex flow and a Burgers vortex flow that are used to model large-scale and small-scale vortex flows in turbulence, respectively [24,25]. Vilela and Motter [26] showed that permanent trapping of inertial aerosols much heavier than the advecting fluid can occur in two widely studied open flows: the blinking vortex system with static vortices and the leapfrogging vortex system with moving vortices. Recently, Sapsis, and Haller [27] performed an analysis to predict the location of inertial particle clustering in three-dimensional steady or two-dimensional time-periodic flows. Angilella [28] examined trapping of dust particles in an inviscid vortex pair with equal strength and revealed that permanent trapping at two attracting points can occur for heavy particles injected in an isolated corotating vortex pair. For similar trapping with unequal vortex strength, Nizkaya *et al.* [29] found that dust particles can be captured by attracting equilibrium points in a corotating vortex pair and trapped by a limit cycle in a counter-rotating vortex pair. Although these prior studies have revealed abundant dynamic features in particle entrainment and trapping, the underlying mechanisms are simply the balance between the centrifugal force due to particle inertia (that pushes the particles outward) and the hydrodynamic force exerted by vortex flow (that drives the particles toward the vortex center). The use of the inward hydrodynamic force in accomplishing particle trapping can be enhanced by the unsteadiness and turbulence of a vortex flow.

In contrast to the aforementioned particle transport mechanisms, particle trapping at a localized location is unique to microfluidics with vanishing particle inertia, steady Stokes fluid flows, and various short-range effects such as electrostatic forces or dielectrophoresis (DEP). We have undertaken this problem and demonstrated theoretically that steady EOF vortices can indeed act as long-range collectors to facilitate particle trapping by short-range forces [30]. In

this study, the vortices were generated by a pair of oppositely charged strips in an unbounded fluid. One can also combine the effects of patterned surface charge with hydrodynamic flow to form closed recirculating EOF rolls [31]. Geometry effects might also help to generate desired structures of EOF vortices, as occurring in an open charged cavity [32]. The deficiency in particle trapping is that it would take a long time for such vortex flows to bring particles at a distance down onto the collecting surface.

Perhaps a more efficient way is to trap particles by confined EOF vortices in a closed environment in which flow depletion effects can be completely eliminated. This confinement-assisted trapping has been demonstrated by active deposition of particles on patterned, energized electrodes inside a sessile droplet with combined effects of EOF and evaporation [33]. We expect that similar but more robust trapping might take place using confined ICEO or ACEO vortices.

In this paper, we aim at providing feasible techniques for particle trapping, release, and sorting by confined EOF microvortices. In particular, we seek not only to delineate the conditions for a vortex trap, a point trap and a limit cycle trap, but also to suggest a means to sort different particles. Starting with the Stokes flow equation and general boundary conditions, we derive an analytical solution for two-dimensional microvortex flow within a semicircular cap in Sec. II. We also utilize this solution to illustrate the structures of confined microvortex flows under the no-slip and free-slip boundary conditions. In Sec. III, kinetic equations are presented to govern particle motion under various velocity and force fields. In Sec. IV, we develop a generic bifurcation theory to identify dynamic characteristics of particle motion in a vortex. This theory offers a facile way to break a vortex trap, create a point trap, or generate a limit cycle trap, providing an adroit manipulation of particle trapping and release. In particular, we find that the formation of a point or limit cycle trap is sensitive to particle identity. This feature is advantageous to sort colloidal particles as explored in Sec. V. This work is concluded in Sec. VI.

II. MATHEMATICAL FORMULATION AND SOLUTION FOR STOKES FLUID FLOW IN A SEMICIRCULAR CHANNEL

As depicted in Fig. 1, we consider the two-dimensional microfluidic flow in a semicircular cap driven by a nonuniform distribution of the electrokinetic (or Smoluchowski) slip velocity on the bottom surface. Assume that the fluid is incompressible and Newtonian, and its flow is Stokes flow at a very low Reynolds number. To interpret the problem in dimensionless form, we scale velocity and length by the maximum Smoluchowski slip velocity U_0 and the radius of the semicircle L , respectively. Pressure and stress are scaled by $\mu U_0/L$, where μ denotes the viscosity of fluid.

A. Analytical solution for general microfluidic flow

For Stokes flow, the stream function ψ in the polar coordinates (r, θ) satisfies the familiar biharmonic equation

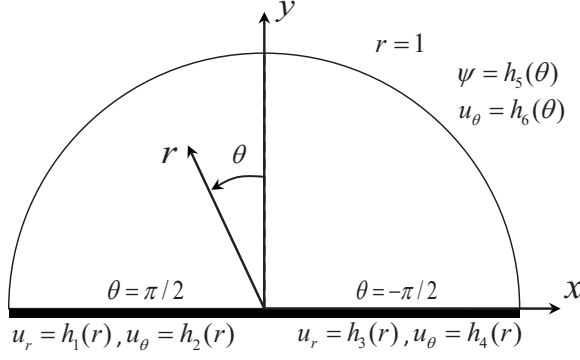


FIG. 1. Geometry of the microfluidic system. In the semicircle, two-dimensional microvortex flow is driven by a nonuniform electrokinetic slip velocity prescribed on the bottom surface.

$$\nabla^4 \psi = 0 \quad (1)$$

and the velocity field (u_r, u_θ) can be readily obtained through

$$u_r = \frac{1}{r} \frac{\partial \psi}{\partial \theta}, \quad u_\theta = -\frac{\partial \psi}{\partial r}, \quad (2a)$$

which satisfy the continuity equation automatically. In the Cartesian coordinates (x, y) , the velocity components u_x and u_y are related to u_r and u_θ via

$$u_x = -u_r \sin \theta - u_\theta \cos \theta, \quad u_y = u_r \cos \theta - u_\theta \sin \theta. \quad (2b)$$

The general boundary conditions are

$$u_r = h_1(r), \quad u_\theta = h_2(r) \quad \text{at} \quad \theta = \pi/2, \quad (3a)$$

$$u_r = h_3(r), \quad u_\theta = h_4(r) \quad \text{at} \quad \theta = -\pi/2, \quad (3b)$$

$$\psi = h_5(\theta), \quad u_\theta = h_6(\theta) \quad \text{at} \quad r = 1. \quad (3c)$$

Equations (3a) and (3b) provide the slip velocity distribution on the bottom surface by virtue of $h_1(r)$ and $h_3(r)$, which are imposed by nonuniform functionalization, ICEO, ACEO, or an external momentum source. Equation (3c) is the inflow/outflow boundary condition on the cap. In this condition, $u_\theta = h_6(\theta)$ can also be replaced by specifying the shear stress $\tau_{r\theta}$ via

$$\tau_{r\theta} = \frac{1}{r^2} \frac{\partial^2 \psi}{\partial \theta^2} + \frac{1}{r} \frac{\partial \psi}{\partial r} - \frac{\partial^2 \psi}{\partial r^2}. \quad (4)$$

Taking the general solution provided by Leal [34] and assuming finite velocity at $r=0$, the solution to Eq. (1) is then composed by a linear combination of four flow modes, $r^\lambda \sin \lambda \theta$, $r^\lambda \cos \lambda \theta$, $r^\lambda \sin(\lambda-2)\theta$, and $r^\lambda \cos(\lambda-2)\theta$, with λ being a real number. The first two modes are irrotational, whereas the latter two modes are rotational. Applying the boundary conditions of Eqs. (3a)–(3c), we arrive at four fundamental solutions. Each of them, satisfying a specific type of homogeneous boundary conditions, is divided into an odd and an even part with respect to θ , *viz.* $\psi_n = \psi_n^{\text{odd}} + \psi_n^{\text{even}}$ (see Appendix A for the proof), as listed below.

(1) $u_\theta = 0$ at $\theta = \pm \pi/2$

$$\psi_1^{\text{odd}} = \sum_{m=2,4}^{\infty} (a_m r^m + b_m r^{m+2}) \sin m\theta, \quad (5a)$$

$$\psi_1^{\text{even}} = \sum_{m=1,3}^{\infty} (a'_m r^m + b'_m r^{m+2}) \cos m\theta. \quad (5b)$$

(2) $u_r = 0$ at $\theta = \pm \pi/2$

$$\psi_2^{\text{odd}} = \sum_{m=1,3}^{\infty} (a_m r^m + b_m r^{m+2}) \sin m\theta, \quad (6a)$$

$$\psi_2^{\text{even}} = \sum_{m=0,2}^{\infty} (a'_m r^m + b'_m r^{m+2}) \cos m\theta. \quad (6b)$$

(3) $u_r = u_\theta = 0$ at $\theta = \pm \pi/2$

$$\psi_3^{\text{odd}} = c_1 r^3 \sin \theta + \sum_{m=3,5}^{\infty} (c_{m-2} r^m + c_m r^{m+2}) \sin m\theta, \quad (7a)$$

$$\psi_3^{\text{even}} = \psi_0 + c'_0 r^2 + \sum_{m=2,4}^{\infty} (c'_{m-2} r^m + c'_m r^{m+2}) \cos m\theta. \quad (7b)$$

(4) $u_r = u_\theta = 0$ at $\theta = \pm \pi/2$ and $\psi = 0$ at $r = 1$

$$\psi_4^{\text{odd}} = \sum_{i=1}^{\infty} \beta_i \psi_{4i}^{\text{odd}}, \quad (8a)$$

$$\psi_4^{\text{even}} = \sum_{i=1}^{\infty} \beta'_i \psi_{4i}^{\text{even}}, \quad (8b)$$

where

$$\begin{aligned} \psi_{4i}^{\text{odd}} = & d_{i1} r^3 \sin \theta + \sum_{k=2}^{\infty} (d_{i,k-1} r^{2k-1} + d_{ik} r^{2k+1}) \sin(2k-1)\theta \\ & - r^{2i+2} \sin 2i\theta + \sum_{k=2}^{\infty} \frac{(-1)^{k-1} i}{k+i-1} (r^{2k+2i-2} - r^{2k+2i}) \\ & \times \sin(2k+2i-2)\theta, \end{aligned} \quad (8c)$$

$$d_{ik} = \sum_{j=1}^k \frac{(-1)^{i+k} (8i)}{\pi(2i+2j-1)(2i-2j+1)}, \quad (8d)$$

$$\begin{aligned} \psi_{4i}^{\text{even}} = & d'_{i1} r^2 + \sum_{k=2}^{\infty} (d'_{i,k-1} r^{2k-2} + d'_{ik} r^{2k}) \cos(2k-2)\theta \\ & - r^{2i+1} \cos(2i-1)\theta + \sum_{k=2}^{\infty} \frac{(-1)^{k-1} (2i-1)}{2k+2i-3} \\ & \times (r^{2k+2i-3} - r^{2k+2i-1}) \cos(2k+2i-3)\theta, \end{aligned} \quad (8e)$$

$$d'_{ik} = \frac{(-1)^{i+k}}{\pi(i-1/2)} + \sum_{j=2}^k \frac{(-1)^{i+k} (8i-4)}{\pi(2i+2j-3)(2i-2j+1)}. \quad (8f)$$

Through a superposition of the above fundamental solutions, we invoke procedures below to systematically derive an analytical solution for the problem.

Step 1. Use the fundamental solution ψ_1 in Eq. (5) to satisfy the slip velocity u_r given by Eqs. (3a) and (3b), i.e., $\partial\psi_1/\partial\theta=rh_1(r)$ at $\theta=\pi/2$ and $\partial\psi_1/\partial\theta=rh_3(r)$ at $\theta=-\pi/2$. Here, we assume that the slip velocity distribution can be well approximated by a polynomial in r with a proper choice of the coefficients a_m , b_m , a'_m , and b'_m .

Step 2. Apply the fundamental solution ψ_2 in Eq. (6) to satisfy u_θ (in terms of a polynomial in r) at $\theta=\pm\pi/2$ also given by Eqs. (3a) and (3b). The coefficients a_m , b_m , a'_m , and b'_m are chosen such that $\partial\psi_2/\partial r=-h_2(r)$ at $\theta=\pi/2$ and $\partial\psi_2/\partial r=-h_4(r)$ at $\theta=-\pi/2$.

Step 3. The solution secured so far is $\psi_1(r, \theta)+\psi_2(r, \theta)$, which satisfies all the boundary conditions of Eqs. (3a) and (3b). The next step is to incorporate the fundamental solution ψ_3 in Eq. (7) to meet the condition of $\psi=h_5(\theta)$ at $r=1$ in Eq. (3c). The coefficient ψ_0 in Eq. (7b) is used to designate the reference value and can be chosen as $[\psi(1, \pi/2)+\psi(1, -\pi/2)]/2$. The coefficients c_m and c'_m are evaluated to make $\psi_3(1, \theta)$ equal to $h_5(\theta)-\psi_1(1, \theta)-\psi_2(1, \theta)$, yielding

$$c_1 = \varphi_1, \quad c_m = \varphi_m - c_{m-2}, \quad m = 3, 5, \dots, \quad (9a)$$

$$c'_0 = \varphi'_0, \quad c'_m = \varphi'_m - c'_{m-2}, \quad m = 2, 4, \dots, \quad (9b)$$

where

$$\begin{aligned} & h_5(\theta) - \psi_1(1, \theta) - \psi_2(1, \theta) - \psi_0 \\ &= \sum_{m=1,3}^{\infty} \varphi_m \sin m\theta + \sum_{m=0,2}^{\infty} \varphi'_m \cos m\theta. \end{aligned} \quad (9c)$$

Step 4. In the final step, the fundamental solution ψ_4 in Eq. (8) is employed to satisfy the last boundary condition $u_\theta=h_6(\theta)$ at $r=1$ in Eq. (3c). Note that the addition of ψ_4 will not alter any boundary conditions employed in the preceding three steps. We can thus determine the expansion coefficients β_i and β'_i in ψ_4 by applying the complete solution, $\psi=\psi_1+\psi_2+\psi_3+\psi_4$, to meet $u_\theta=h_6(\theta)$ at $r=1$.

B. Analytical solution for confined microvortex flow

For the fluid flow confined within in the semicircular cap, we specify the following conditions in Eq. (3) to ensure no flow across the outer boundary,

$$u_\theta = 0 \quad \text{at} \quad \theta = \pm\pi/2, \quad (10a)$$

$$\psi = 0 \quad \text{at} \quad r = 1. \quad (10b)$$

At the cap, we apply either the “no-slip condition” to a solid-liquid interface or the “free-slip condition” to a gas-liquid interface,

$$u_\theta = 0 \quad \text{at} \quad r = 1 \quad \text{for no-slip surface}, \quad (10c)$$

$$\tau_{r\theta} = 0 \quad \text{at} \quad r = 1 \quad \text{for free-slip surface}. \quad (10d)$$

In Eq. (10d), the zero tangential stress condition renders the slippery outer boundary, which can simulate a microfluidic

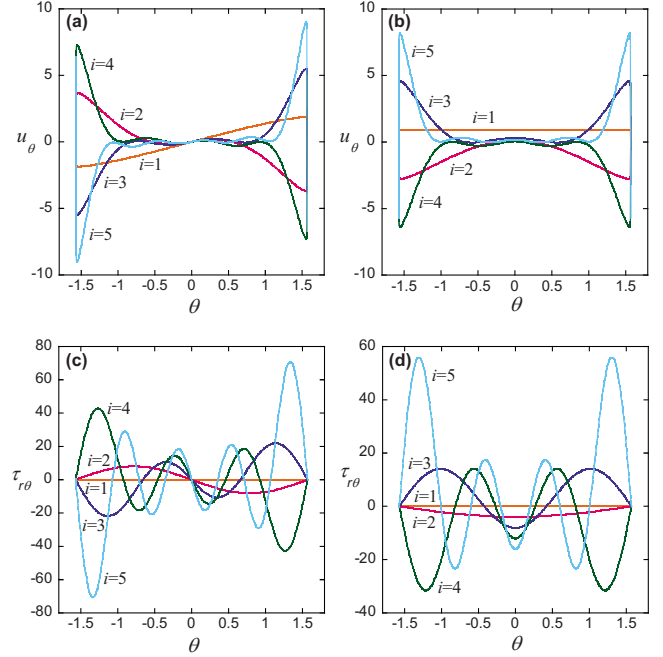


FIG. 2. (Color online) First five sets of functions ψ_{4i}^{odd} are converted to represent u_θ and $\tau_{r\theta}$ at $r=1$ in panels (a, c). Those derived from ψ_{4i}^{even} are shown in panels (b, d).

system involving a droplet of colloidal suspension on a long substrate. Here, the droplet shape is treated approximately as a semicircle and the interface is assumed to be fixed at $r=1$, provided that the surface tension force is sufficiently strong compared to the viscous force, i.e., the capillary number $\text{Ca}=\mu U_0/\gamma \ll 1$ where γ is the surface tension. Other conditions due to an external momentum source could also be used to replace Eq. (10d) at the gas-liquid interface. Note that the functions ψ_{4i}^{odd} and ψ_{4i}^{even} developed in Eqs. (8c) and (8e) can be converted to represent u_θ or $\tau_{r\theta}$, such that the no-slip or free-slip boundary condition can be satisfied. The first five sets of the converted functions are evaluated at $r=1$ and elucidated in Fig. 2.

Confined microvortex flow can be set up by a nonuniform slip velocity $u_{\text{slip}}=u_r$ over the bottom surface at $\theta=\pm\pi/2$ as seen in Eqs. (3a) and (3b). The distribution of this velocity can be approximated by a polynomial in x as follows:

$$u_{\text{slip}} = u_x|_{y=0} = \sum_{j=0}^M p_j x^j. \quad (11)$$

The detailed derivation of the analytical solution is provided in Appendix B. Below, we illustrate the use of the analytical solution with an example.

Example 1. For the no-slip and free-slip microvortex flows, we obtain analytical solutions with $N=10$ (see Appendix B for the use of N) when the following slip velocity distribution is imposed over the bottom surface ($-1 \leq x \leq 1$ and $y=0$):

$$u_{\text{slip}}(x) = 0.444(1 - 4x - x^2 + 4x^3).$$

This velocity is zero at $x=0.25$, positive for $x<0.25$, and negative for $x>0.25$, which might mimic situations occur-

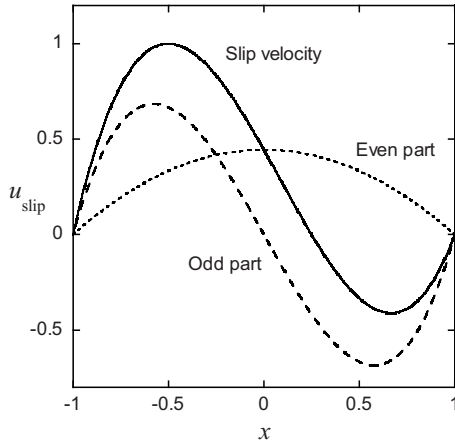


FIG. 3. Nonuniform slip velocity over the bottom surface for Example 1. The slip velocity can be decomposed into its odd and even parts.

ring in ACEO. As elucidated in Fig. 3, each analytical solution can be decomposed into odd and even parts by splitting $u_{\text{slip}}(x)$ into $u_{\text{slip}}^{\text{odd}}(x)$ and $u_{\text{slip}}^{\text{even}}(x)$, respectively. Each odd part generates a pair of counter-rotating vortices in equal sizes, as shown in Figs. 4(c) and 4(d). Each even part generates a single vortex, circulating across the entire semicircle, as seen in Figs. 4(e) and 4(f).

Combining the odd and even parts, Figs. 4(a) and 4(b) show the streamlines of vortex flow patterns subject to the

no-slip and free-slip conditions, respectively. The results reveal a pair of asymmetric microvortices separated by a dividing dotted line emitted from the stagnation point (at $x=0.25$) on the bottom surface where the fluid velocity vanishes. Note that the positive slip velocity, which is larger in magnitude, causes the larger counterclockwise vortex on the left. In addition, since the flow comes toward the stagnation point from both sides along the surface, it constitutes a converging stagnation point that is particularly useful for particle trapping. Moreover, it seems that the centers of the vortices in the no-slip case are closer to the bottom surface. This flow feature might aid in capturing particles at the stagnation point as will be elaborated later.

III. SINGLE PARTICLE MOTION IN A MICROVORTEX FLOW FIELD

To realize particle transport in a vortex, we need to derive kinetic equations to describe particle motion under various velocity and force fields. We limit this study to the dilute concentration regime, in which particle-particle interactions are neglected. Hence, for a small rigid spherical particle of radius R instantaneously centered at $[x_p(t), y_p(t)]$ and moving with velocity $V_i(t)$, we first consider the dimensionless equation governing particle motion in the undisturbed flow field u_i as follows:

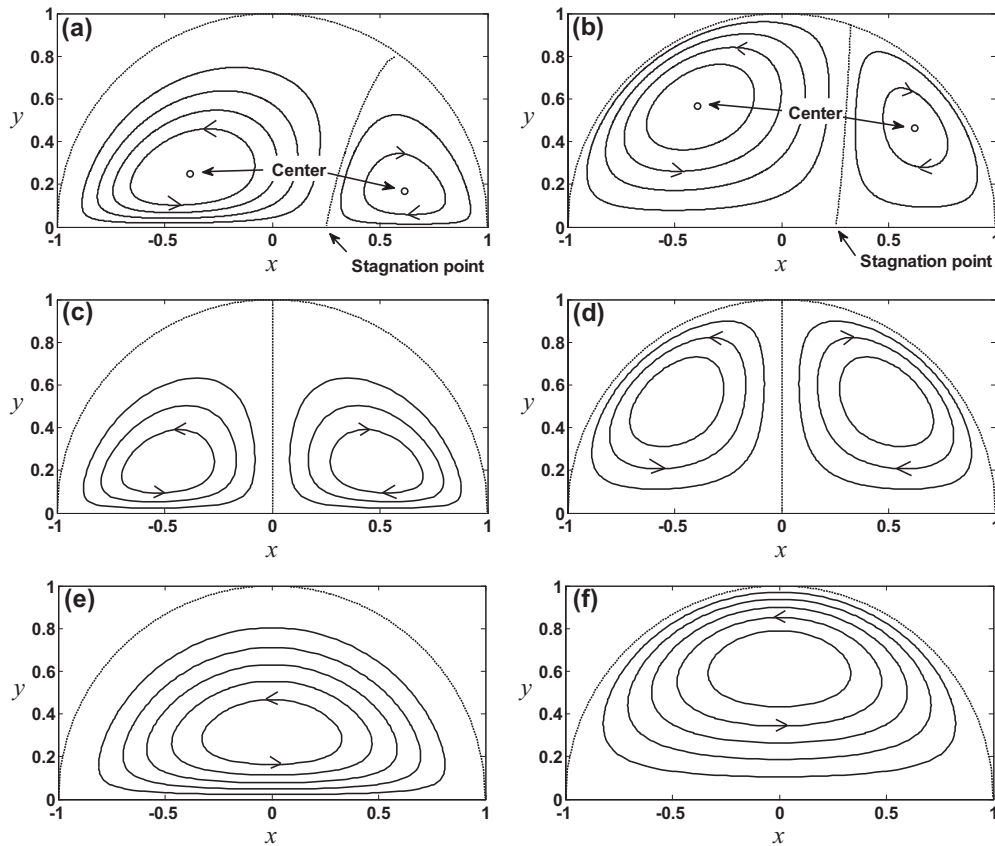


FIG. 4. Respective flow structures generated by the slip velocity, its odd part and its even part depicted in Fig. 3: (a, c, e) under the no-slip condition; (b, d, f) under the free-slip condition. Vortex flow structures in panels (a, b) show converging stagnation points on the bottom surface.

$$\begin{aligned} \text{St} \frac{dV_i}{dt} = & \frac{\rho_f \text{St} Du_i}{\rho_p} - \frac{\rho_f \text{St}}{2\rho_p} \left[\frac{dV_i}{dt} - \frac{D}{Dt} \left(u_i + \frac{3\text{Fa}}{5} \nabla^2 u_i \right) \right] \\ & + \text{Ga} e_i - (V_i - u_i - \text{Fa} \nabla^2 u_i) \\ & - \text{Ba} \int_0^t \frac{1}{\sqrt{t-\tau}} \frac{d}{d\tau} (V_i - u_i - \text{Fa} \nabla^2 u_i) d\tau. \end{aligned} \quad (12)$$

In the equation above, time has been scaled by L/U_0 , the subscript i can be x or y and e_i denotes the unit vector pointing downward in the vertical direction (the direction of gravity). The derivatives d/dt and D/Dt denote time derivatives following a moving sphere and a fluid element, respectively. The terms on the right correspond in turn to the force exerted by the undisturbed flow, the added mass, buoyancy, Stokes drag, and the Basset history force. The $\nabla^2 u_i$ term represents the Faxen correction to the Stokes drag force due to local variations of the flow field around the particle, and comes only from the rotational part of fluid flow. Equation (12) was first derived by Maxey and Riley [20], except for the added-mass term, whose form was corrected by Babiano *et al.* for targeting trajectories of small neutrally buoyant particles [35].

The four dimensionless parameters in Eq. (12) are the particle Stokes, gravity, Faxen, and Basset numbers as given, respectively, by

$$\text{St} = \frac{2R^2 \rho_p U_0}{9\mu L}, \text{Ga} = \frac{2R^2(\rho_p - \rho_f)g}{9\mu U_0}, \text{Fa} = \frac{R^2}{6L^2}, \text{Ba} = R \sqrt{\frac{\rho_f U_0}{\pi\mu L}},$$

where ρ_p is the particle density, ρ_f the fluid density, and g the gravitational acceleration. The Stokes number St can be interpreted as the ratio of the dynamic response time of the particle ($2R^2\rho_p/9\mu$) to the time scale associated with the fluid motion (L/U_0). A small value of the Stokes number implies that the particle behavior is dominated by the viscous force.

To simplify the dynamic analysis of particle motion, we assume that St is so small that the particle inertial term, the force exerted by the undisturbed flow, and the added-mass term can be ignored. Moreover, we postulate two situations for the Faxen correction and Basset history terms subsequently. First, Fa and Ba are such small numbers that both terms are negligible. To be more quantitative, we consider the specific case of spherical particles ($R=5 \mu\text{m}$, $\rho_p=1.1 \text{ g/cm}^3$, $g=980 \text{ cm/s}^2$) suspended in water ($\rho_f=1 \text{ g/cm}^3$, $\mu=0.01 \text{ g/cm s}$, $U_0=100 \mu\text{m/s}$) on a substrate ($L=200 \mu\text{m}$). The four dimensionless parameters are calculated as $\text{St}=3.06 \times 10^{-6}$, $\text{Ga}=0.0544$, $\text{Fa}=1.04 \times 10^{-4}$, and $\text{Ba}=0.0020$. It appears that merely the gravitational and viscous terms are significant in Eq. (12). The second situation assumes $\text{Ba} \ll \text{Fa}$ so as to retain the Faxen effect but ignore the Basset history term. This would result in the undesirable feature of a very small vortex velocity ($U_0 \ll \mu R^2/\rho_f L^3$). We thus restrict the second situation to investigation on settling by gravity in the absence of other external forces.

Based on the above postulations, the following kinetic equations are established for particle motion:

$$\frac{dx_p}{dt} = u_x + \text{Fa} \nabla^2 u_x + Z_D E_{D,x} + Z_N E_{N,x} \equiv F[x_p(t), y_p(t)], \quad (13a)$$

$$\frac{dy_p}{dt} = u_y + \text{Fa} \nabla^2 u_y - \text{Ga} + Z_D E_{D,y} + Z_N E_{N,y} \equiv G[x_p(t), y_p(t)]. \quad (13b)$$

The u_i terms reflect the particle's movement advected by the fluid flow. The newly added terms account for the effects of other external forces acting on the particle. Such forces are divided into the divergence-free (DF) part $E_{D,i}$ and the nondivergence-free (NDF) part $E_{N,i}$ multiplied by the respective nondimensional mobilities Z_D and Z_N . The DF part can come from electric, optical, or magnetic forces. On the other hand, electrostatic or dielectrophoretic interactions between the particle and the bottom surface can contribute to short-range NDF forces on the particle when it is close to the surface. Note that both fluid velocity and gravity are divergence-free because the former satisfies the continuity equation and the latter is a uniform and unidirectional field. Moreover, any particle motion caused by a DF force field can be described by a stream function. For instance, $\psi=r \sin \theta$ stands for the uniform field of $u_x=0$ and $u_y=1$, whereas $\psi=r \cos \theta$ stands for the uniform field of $u_x=1$ and $u_y=0$.

IV. MECHANISMS FOR PARTICLE TRAPPING AND RELEASE IN MICROVORTICES

In this section, we seek to understand particle trapping and release mechanisms at a stagnation point on the bottom surface as well as via a point or a limit cycle trap in the circulating fluid. In particular, we would like to illuminate the role of a nondivergence-free force and discuss the conditions necessary for particle trapping and release.

A. Linear stability analysis of particle flow

We first carry out a linear stability analysis for the dynamic system given by Eq. (13) at some fixed point (\bar{x}_p, \bar{y}_p) . This analysis not only enables us to identify the dynamic nature of the fixed point, but also tell us how to modify its stability for manipulating the nonlinear behavior of particle flow. The fixed point satisfies the equilibrium condition

$$F(\bar{x}_p, \bar{y}_p) = G(\bar{x}_p, \bar{y}_p) = 0. \quad (14)$$

The eigenvalues λ_{\pm} of the Jacobian matrix $\mathbf{J}(\bar{x}_p, \bar{y}_p)$ can be calculated by

$$\lambda_{\pm} = \frac{1}{2} [\text{tr}(\mathbf{J}^*) \pm \sqrt{\text{tr}(\mathbf{J}^*)^2 - 4 \det(\mathbf{J}^*)}]. \quad (15a)$$

Here, the superscript $*$ denotes the value evaluated at the fixed point, and the trace and determinant of the matrix are given by

$$\text{tr}(\mathbf{J}^*) = \frac{\partial F^*}{\partial x_p} + \frac{\partial G^*}{\partial y_p}, \quad (15b)$$

$$\det(\mathbf{J}^*) = \frac{\partial F^*}{\partial x_p} \frac{\partial G^*}{\partial y_p} - \frac{\partial F^*}{\partial y_p} \frac{\partial G^*}{\partial x_p}. \quad (15c)$$

We see from Eq. (15b) that if all the velocity and force fields in Eq. (13) are divergence-free, i.e., $E_{N,i}=0$, the trace is always zero. In this case, Eq. (15a) suggests that the corresponding fixed point can be either a saddle point having two real eigenvalues of the same absolute value but opposite signs or a center having a pair of purely imaginary eigenvalues. However, the addition of a nondivergence-free force field $E_{N,i}$ could make the trace nonzero and hence turn a center fixed point into a stable or unstable spiral. This feature allows us to trap or release particles with the aid of repulsive or attractive NDF forces.

B. Vortex trap in a divergence-free field

In the absence of NDF forces, a center fixed point for particle flow often exists within a fluid vortex. It is found that this center is accompanied by a vortex trap in which every particle circulates along its specific isolated and closed path and permanently suspends there (see Appendix C for the derivation of the normal form). This phenomenon is in line with that observed by Stommel [36] for noninertial particles settling in a cellular flow field. The vortex trap often prevents particle trapping at a fixed point because it can neither capture particles from the outside nor release particles from the inside.

A permanent vortex trap for particles is difficult to realize in reality. Rubin *et al.* [21] applied a singular perturbation theory to show that a small amount of inertia is sufficient to break the closed orbits of the particles and causes them to settle eventually. Nevertheless, under the assumptions of vanishing particle inertia and no NDF force, the enclosed particles would escape away from the closed orbits very slowly and could be treated essentially as being confined.

C. Particle trapping at a converging stagnation point without NDF force

As demonstrated by previous studies [2,30,37], a stagnation point with converging fluid flow occurring on a surface can be used to facilitate particle trapping, especially with the aid of short-range attractive forces. The advantage of such a manipulation is that vortex flow provides long-range convective transport that rapidly conveys suspended particles to the proximity of the collecting surface. Those particles are then brought onto the surface by certain short-range effects against upward fluid flow. Finally, particle focusing is realized by surface slip streams toward the stagnation point.

We intend to explore the efficiency or speed of particle trapping at the converging stagnation point in vortex-pair structures developed in Example 1. Here, the trapping efficiency must be distinguished from the trapping speed. The former measures how many particles can be trapped, whereas the latter concerns how fast the particles are trapped. We first investigate the trapping efficiency at the stagnation point subject to the DF Faxen and gravitational forces using Eq. (13) with $Z_D=Z_N=0$.

Figure 5 elucidates the impact of the Faxen effect (Fa)

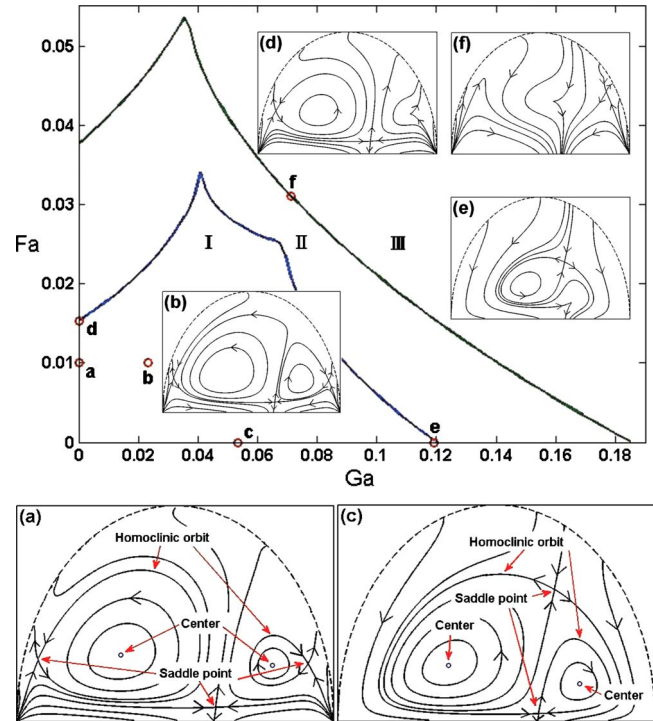


FIG. 5. (Color online) Effects of Fa and Ga on the efficiency of particle trapping at the stagnation point in the no-slip vortex flow of Example 1. Panels (a-f) depict different particle dynamics corresponding to the open circles indicated in the upper panel. Note that the aspect ratio of each semicircle has been varied to exhibit particle dynamics more clearly.

and gravity (Ga) on the efficiency of particle trapping at the stagnation point in the no-slip vortex flow of Example 1. In the parameter space of Fa and Ga , the figure shows two bifurcation curves that partition the space into three regions (I–III), which possess different phase portraits of particle flow and hence different trapping characteristics as depicted in Figs. 5(a)–5(f). Recall that a vortex trap accompanies a center with the eigenvalues of $\pm j\omega$. Each bifurcation curve is a collection of double-zero bifurcation points, at which the center of a vortex trap becomes a fixed point with two zero eigenvalues, viz. $\omega=0$. It is found that the vortex trap dwindles in size with a decrease in ω and eventually vanishes as ω is reduced to zero. Consequently, there are two vortex traps in region I, one vortex trap in region II, and no vortex trap in region III.

Figures 5(a)–5(c) in region I reveal that each of the two vortex traps is enclosed by a homoclinic orbit, which joins a saddle point to itself. Hence, the size of a vortex trap can be roughly estimated by the distance between the center and the connecting saddle point. The right vortex trap (the smaller one) vanishes at the first bifurcation curve as evidence in Figs. 5(d) and 5(e), whereas the left vortex trap (the larger one) vanishes at the second bifurcation curve as seen in Fig. 5(f).

The operation conditions belonging to region I are commonly encountered in practice (small Fa and Ga) and are worth special attention. From Fig. 5(a), which corresponds to point (a) at $Fa=0.01$ and $Ga=0$ (ignoring gravity), we see

that the Faxen effect elicits at least three saddle points of particle motion. The middle saddle point lies slightly above the stagnation point; any particle abiding below the stable manifold of this saddle point will be brought onto the bottom surface and then focused at the stagnation point by surface streams. The left and right saddle points form two vortex traps that confine particles inside. The rest of the particles will be driven elsewhere. It follows that the Faxen effect in the no-slip vortex flow provides a positive but limited capacity to facilitate particle trapping. On one hand, the middle saddle point help collect a part of the particles, and on the other hand, it restrains the rest of the particles from being captured by the stagnation point.

This deficiency caused by the Faxen effect can be improved by gravity as illustrated by Fig. 5(b) at $Fa=0.01$ and $Ga=0.0231$ and Fig. 5(c) at $Fa=0$ and $Ga=0.0533$ (ignoring the Faxen effect). With an increase in gravity, the original connection of the left homoclinic orbit with the left saddle point as shown in Fig. 5(a) is broken and a new connection is established with the middle saddle point as seen in Fig. 5(b). This allows more particles on the left and outside the left vortex trap to settle on the bottom surface. A further increase in gravity will force the two homoclinic orbits to reconnect with the upper and lower saddle points as indicated in Fig. 5(c). As a result, almost all particles except those confined in the two vortex traps will be trapped at the stagnation point. This implies that when the gravity is dominant ($Ga \gg Fa$), the trapping efficiency at the stagnation point can be evaluated by the size of the vortex trap(s) as is evidenced in Figs. 5(c), 5(e), and 5(f) in the three regions.

Note that an increase in the divergence-free force of the Faxen effect or gravity does not break the vortex trap instantly by varying the stability of the center but can shrink its size and release more particles. The disappearance of the vortex trap, however, requires a sufficiently large Faxen or gravitational force as shown in regions II and III.

Figure 6 elucidates the impact of the Faxen effect and gravity on the efficiency of particle trapping at the stagnation point in the free-slip vortex flow of Example 1. The parameter space is divided into three regions (I–III) by two double-zero bifurcation curves (solid lines) and is partitioned into two regions (A and B) by a dashed line. Note that the dashed line can be approximated by $Fa \approx 0.1 Ga$. Therefore, regions A and B can be determined by $\rho_p - \rho_f < 7.5\mu U_0 / gL^2$ and $\rho_p - \rho_f > 7.5\mu U_0 / gL^2$, respectively. This figure consists of six subregions (IA–IIIA, IB–IIIB), each of which possesses a specific phase portrait of particle flow as depicted in Figs. 6(a)–6(g). In contrast with the no-slip case, the Faxen effect here would induce upward particle transport from the bottom surface because it cannot elicit a saddle point above the stagnation point as indicated in Figs. 6(a) and 6(d). Therefore, any particles near the stagnation point will be dispersed away by the induced upward motion. The dashed line in Fig. 6 denotes the situation where the gravity compensates for the Faxen effect so as to induce a saddle point right on the bottom surface. Consequently, particles cannot be trapped at the stagnation point in region A because of the negative outcome of the Faxen effect as is clearly revealed in Fig. 6(f). This shortcoming can be remedied by the presence of gravity. In subregions IB–IIIB, which are to the right of the dashed line,

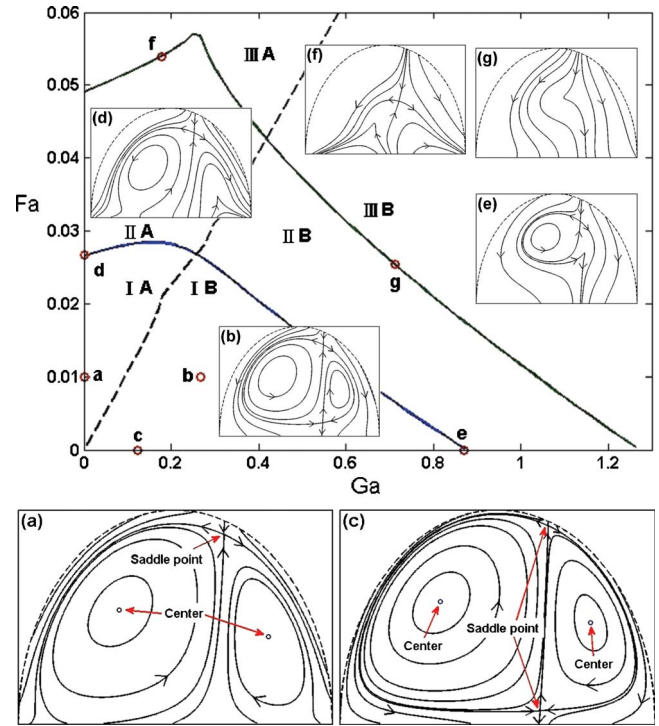


FIG. 6. (Color online) Effects of Fa and Ga on the efficiency of particle trapping at the stagnation point in the free-slip vortex flow of Example 1. Panels (a–g) depict different particle dynamics corresponding to the open circles indicated in the upper panel.

particle trapping at the stagnation point is realizable in the presence of sufficient gravity. The trapping characteristics as shown in Figs. 6(b), 6(e), and 6(g) are qualitatively similar to those seen in Figs. 5(c), 5(e), and 5(f) for the no-slip case. Nevertheless, under the same gravity, the no-slip vortex flow produces much better trapping efficiency than the free-slip vortex flow.

D. Particle trapping at a stagnation point with NDF force

Figures 5(b) and 6(b) reveal that the presence of large vortex traps could deteriorate the trapping efficiency at a stagnation point by holding more particles inside. To promote the trapping efficiency in Example 1, one can turn the center fixed point of a vortex trap into an unstable spiral with an attractive NDF force. Such a change to instability could break immediately the vortex trap and release particles away from the unstable spiral. As mentioned in Sec. III, if such an NDF force enters as short-range electrostatic or dielectrophoretic attraction between the particle and the surface, it can only act on the particle in the y direction according to

$$E_{N,x} = 0, \quad E_{N,y} = -\exp(-y_p/\delta).$$

The electrostatic force here with the mobility Z_N is given by the screened Coulomb attraction of a charged particle to an oppositely charged surface if the particle comes close to the surface within a certain distance of the electric double layer δ [38]. Because of the charge screening, the force must attenuate exponentially in y at the rate of δ^{-1} according to the Debye-Hückel theory [39]. As for the DEP force, it comes to

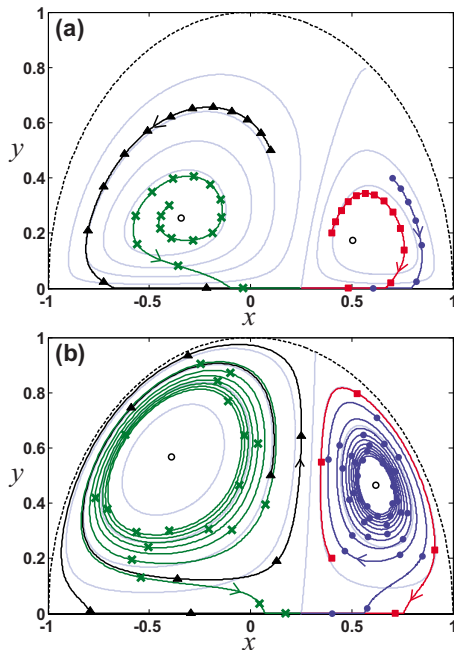


FIG. 7. (Color online) Facilitated particle trapping at the stagnation point due to an attractive NDF force from the bottom surface for Example 1: (a) no-slip vortex flow with $Z_N=0.356$; (b) free-slip vortex flow with $Z_N=0.71$. The vortex flow of fluid is denoted by undertone streamlines, the unstable spiral points are indicated by open circles, and particle trajectories are represented by solid lines. In panels (a, b), particles labeled by the same symbol are placed at the same initial locations. Any two adjacent symbols along each particle trajectory are separated by a time interval of L/U_0 .

attract the particle toward the surface through positive DEP if the field at the surface is the greatest. It can be shown that the local electric field near the surface behaves like $\exp(-y/\kappa)$ with κ measuring the penetration depth of the field. The resulting DEP force is then proportional to $\exp(-y/\delta)$ with $\delta=\kappa/2$, which also decays exponentially in y but at the rate twice faster than the electric field.

With the attractive NDF force to break the vortex traps and release all the enclosed particles, the trapping efficiency at the stagnation point is no longer an issue. We then pay attention to the trapping speed of the no-slip and free-slip designs. To see the effects of the above short-range force with $\delta=0.1$ on particle trapping, we ignore the Faxen correction and gravity and integrate Eq. (13) numerically to calculate particle trajectories in the no-slip vortex flow with $Z_N=0.356$ and in the free-slip vortex flow with $Z_N=0.71$, as shown in Figs. 7(a) and 7(b), respectively. The particle flow scenario is then as follows. Four particles, placed initially in the fluid vortices, move in spiral motion away from the unstable spirals. When any particle come in proximity of the bottom surface, it will perceive more pronounced attraction and hence will be brought onto the surface with an abrupt change in motion. Upon being captured by the surface, the particle is advected horizontally along with the slip flow toward the stagnation point (assuming its normal velocity vanishes).

To see more clearly how fast these particles move, the symbols labeled along the particle trajectories in Fig. 7 are

used to track the particle locations at different times. On each trajectory, any two adjacent symbols indicate the consecutive particle positions during a time interval of L/U_0 . Obviously, the trapping speed can be affected by the traveling velocity and distance of particles. The traveling distance is largely determined by the positions of the unstable spirals above the bottom surface. However, the effect of the traveling distance would dominate over the effect of the traveling velocity due to the short-range nature of the applied force as depicted below. Figure 7(b) for the free-slip design reveals that the two unstable spirals are far away from the bottom surface providing the short-range NDF force and hence experience weak attraction. Consequently, most particles would take a long path to the surface. This becomes more apparent for those trajectories near the spirals, as illustrated by the blue and green particles (labeled, respectively, by circle and x), whose collection is time-consuming. On the other hand, particles away from the unstable spirals will land on the surface quickly because of their fast velocities, as shown by the red and black particles (labeled, respectively, by square and triangle). In contrast, the no-slip design as elucidated in Fig. 7(a) results in two unstable spirals much closer to the bottom surface. As a result of strong attraction, the distance that each particle will travel before landing is significantly shortened. Overall, the no-slip design has a faster trapping speed than the free-slip design even though the strength of the applied NDF force is halved for the no-slip design.

It is worthwhile to emphasize that vortex-based particle trapping is a collaborative mechanism of convective transport and force effects. Hence, its efficiency and speed depend on the detailed flow structure and the nature of forces. In this example, the no-slip vortex flow seems to be more effective than the free-slip vortex flow in collecting particles at the converging stagnation point. On the other hand, a DF force such as gravity is less effective in that it cannot break but only shrink a vortex trap in contrast with an NDF force.

E. Particle capturing by a point trap in a vortex flow

The present design applies a repulsive NDF force to create a point trap in a circulating fluid via turning the center of a vortex trap into a stable spiral. Its location is determined mainly by the vortex flow structure and can be varied to a certain extent by various DF and NDF force fields. However, its stability, relating to the trapping speed, can only be changed by an NDF force. It is observed that the location of a point trap is restricted to a small region around the center of a fluid vortex, beyond which the corresponding stable spiral, turning to a saddle point, would lose the capability of collecting particles. If this location is distant from the force source and can only experience weak NDF force, the trapping speed will become inevitably low. Note that the basin of attraction of a point trap could be as large as the entire semi-circle if it were properly designed. We illustrate such a design with an example.

Example 2. Consider a clockwise single vortex flow established by the slip velocity distribution

$$u_{\text{slip}}(x) = -0.844(1 - x - x^2 + x^3).$$

The flow structures under the no-slip and free-slip conditions are portrayed as undertone streamlines in Figs. 8(a) and 8(b),

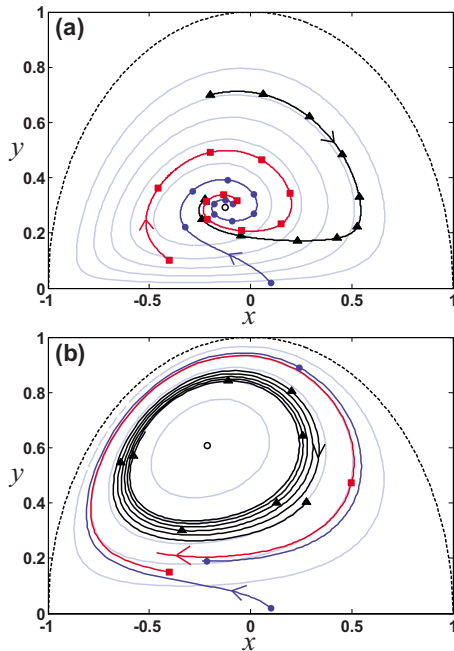


FIG. 8. (Color online) Particle trapping at a point trap (indicated by an open circle) in a single vortex flow (denoted by undertone streamlines) due to a repulsive force from the surface for Example 2: (a) no-slip flow with $Z_N=0.675$; (b) free-slip flow with $Z_N=0.675$. Along each particle trajectory, any two adjacent symbols are separated by a time interval of L/U_0 .

respectively. To generate a point trap, a short-range repulsive NDF force field is placed near the surface according to

$$E_{N,x}=0, \quad E_{N,y}=\exp(-y_p/0.1).$$

Such a repulsive force can again be furnished by electrostatic interactions between a charged particle and a like-charge surface. It can also arise from negative DEP in which a polarized particle can migrate toward low fields under actions of field gradients.

For particles with mobility $Z_N=0.675$ in the no-slip flow, the location of the point trap is indicated as a small open circle in Fig. 8(a). The point trap is rather close to the bottom surface, implying that the NDF force from the surface would exert strong repulsion on the point trap to induce a fast stable spiral. The real-time scenario of particle flow is clearly elucidated by each trajectory along which symbols of the same shape are used to mark the consecutive particle positions during a time interval of L/U_0 . It appears that the trapping speed is fast in that three particles from different places are attracted and soon aggregated near the point trap. Moreover, the trapping efficiency of this design is high because the most adjacent saddle point, limiting the basin of attraction of the point trap, is at a long distance.

For particles with the same mobility in the free-slip vortex flow, the point trap is located rather far away from the surface as seen in Fig. 8(b). It seems that the NDF field given above attenuates very quickly in the direction toward the point trap and hence imparts weak repulsion on it. In other words, the short-range nature of the repulsive force renders the point trap less effective for particle trapping. Evidently,

the trapping speed is low for this design in which the particles are sucked toward the point trap in a slow spiral manner.

F. Particle trapping and release by a limit cycle trap in a vortex

To generate a ring trap, we utilize the well-known phenomenon of a supercritical Hopf bifurcation in which stable limit cycles emerge from a fixed point. It can be shown that for particle motion governed by Eq. (13) in any DF field, a fixed point of center type is accompanied by a pair of purely imaginary eigenvalues and the vanishing first Lyapunov coefficient of $\alpha=0$ (see Appendix C). However, a supercritical Hopf bifurcation requires that the center fixed point should possess a negative α and lose its stability with changes in some parameters [40]. These conditions can be achieved by incorporating a pair of repulsive and attractive NDF force fields, $\xi_r E_{r,i}$ and $\xi_a E_{a,i}$, i.e., replacing $E_{N,i}$ in Eq. (13) by

$$E_{N,i}=\xi_r E_{r,i}+\xi_a E_{a,i}.$$

We then choose $\xi_r=\xi_r^*$ and $\xi_a=\xi_a^*$ such that the fixed point of a particle with mobility Z_N is of center type and the corresponding α is negative. The search for such a setup is straightforward, inasmuch as the center of a fluid vortex is a natural candidate for the desired fixed point. Upon acquiring the supercritical Hopf bifurcation point, the final design is achieved by decreasing the value of ξ_r from ξ_r^* to induce a stable limit cycle with the ring size roughly proportional to $\sqrt{\xi_r^*-\xi_r}$. This ring trap then appears as an orbitally stable limit cycle surrounding an unstable spiral. Note that any DF velocity or force fields cannot contribute to the formation of a limit cycle because they can vary neither the stability of the fixed point nor the value of α .

Figure 9(a) exhibits the typical phase portrait of a stable limit cycle for particle motion within a fluid vortex. The fixed point is an unstable spiral, whereas the closed limit cycle orbit is plotted by the dashed line. This limit cycle will capture particles enclosed by the stable manifold of the neighboring saddle point. Each of them will follow a spiral path toward the closed orbit. The size of the limit cycle is restricted by the neighboring saddle point produced by the counteraction of the applied force and vortex flow. In other words, if the applied NDF force fields are sufficiently strong (e.g., decreasing the value of ξ_r further), the induced limit cycle might extend across the saddle point and be broken by its unstable manifold as shown in Fig. 9(b). Hence, particles in the interior will be brought away or released along the unstable manifold. These behaviors of particle motion will be elaborated later.

V. PARTICLE SORTING USING POINT OR LIMIT CYCLE TRAPS IN VORTICES

Conventional vortex-based particle manipulation is more effective in particle trapping than in particle sorting. The reason is that the vortex flow is mainly employed to bring particles down onto the surface. After the particles land on the surface, the sole role of liquid flow is merely focusing

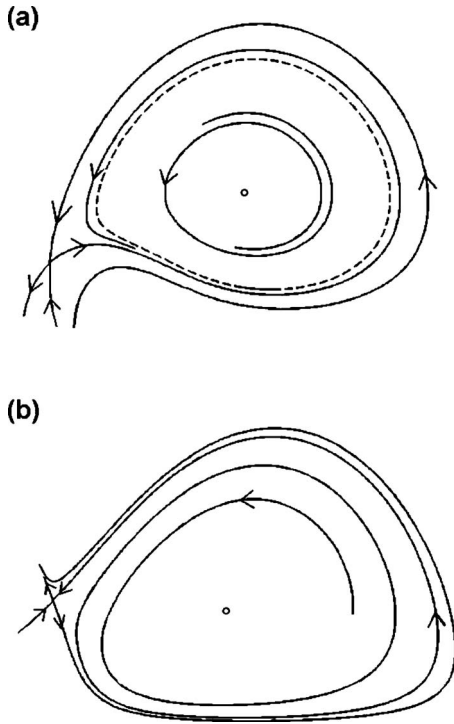


FIG. 9. Typical phase portraits for a stable limit cycle (dashed line) in conjunction with a saddle point, including (a) their existence and (b) the breaking mechanism.

these particles toward the stagnation point, regardless of particle identity (such as size, density, charge, conductivity, etc.), and hence is of little help to particle separation or sorting. On the contrary, the use of point traps or limit cycle traps furnishes an effective means to sort particles because their locations and existence are sensitive to the nature of nonhydrodynamic forces involved and determined exclusively by particle properties. Hence, if there are particles with different properties, it is possible to sort them by the vortex flow into different point traps or limit cycle traps. Recall in Fig. 9(b) that particles with certain properties could break these traps. This suggests that if traps exist for some particles but not for other, complete particle sorting can be realized by capturing those specific to the traps and diverting unspecific ones away.

Below we provide two examples to demonstrate the use of point traps or limit cycle traps in sorting particles through their differences in the mobilities of nonhydrodynamic force fields, Z_D and Z_N , or according to their sizes reflected by gravity Ga .

A. Particle sorting using point traps—Example 3

We start with illustrating particle sorting using point traps in a counterclockwise single vortex flow driven by the slip velocity distribution

$$u_{\text{slip}}(x) = 0.844(1 - x - x^2 + x^3).$$

Both no-slip and free-slip vortex flows are considered to examine the effects of flow structures on the sorting mechanism. To create point traps, a short-range repulsive NDF

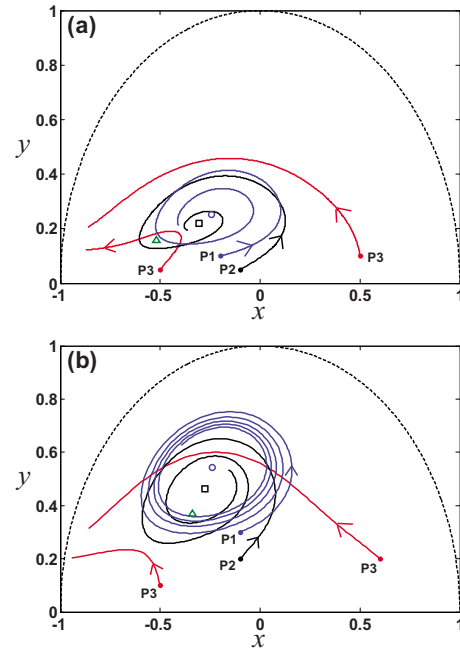


FIG. 10. (Color online) Particle sorting by mobility via point traps (indicated by open circles and squares) for Example 3: (a) no-slip vortex flow with $Z_{D1}=0.127$; (b) free-slip vortex flow with $Z_{D1}=0.506$. The point traps for the critical particle motion leading to complete separation are indicated by triangle symbols.

force field $(E_{N,x}, E_{N,y}) = [0, \exp(-y_p/0.1)]$ is applied to particles with $Z_N=0.169$ for the no-slip case and $Z_N=1.35$ for the free-slip case. To realize sorting by mobility, we impose an additional DF force field $(E_{D,x}, E_{D,y}) = (-1, 0)$ (a uniform force in the horizontal direction) on particles having different DF mobilities Z_D . To realize sorting by size, we postulate that particles of different radii R are subject to the DF force field determined by the gravity number Ga , which is proportional to R^2 .

Figures 10(a) and 10(b) show the trajectories of four particles in the no-slip and free-slip vortex flows, respectively. These particles are of three different types P1, P2, and P3, distinguished by their different mobilities $Z_{D1}:Z_{D2}:Z_{D3} = 1:2:4$. To illuminate how dynamic topology determines the fates of these particles, we place two identical P3 particles at different initial positions.

We find that particles P1 and P2 are sucked to their respective point traps, as indicated by an open circle and an open square. On the contrary, the point trap associated with P3 is now destroyed by the largest DF force of $Z_{D3}E_{D,x}$. That is, the fixed point for the motion of P3 turns to a saddle point. Two P3 particles, starting from different initial positions, will eventually move to the left side of the fluid, and thus be completely separated from particles P1 and P2. Note that particles P1 and P2 will line up in the bulk of the vortex according to their DF mobilities, thus achieving localized separation between them. Extensive numerical simulation studies manifest that the critical particle mobility for achieving complete separation is $3.69Z_{D1}$ for the no-slip case and $3.22Z_{D1}$ for the free-slip case.

Figures 11(a) and 11(b) show the sorting behaviors for three types of particles with different sizes $R_1:R_2:R_3$

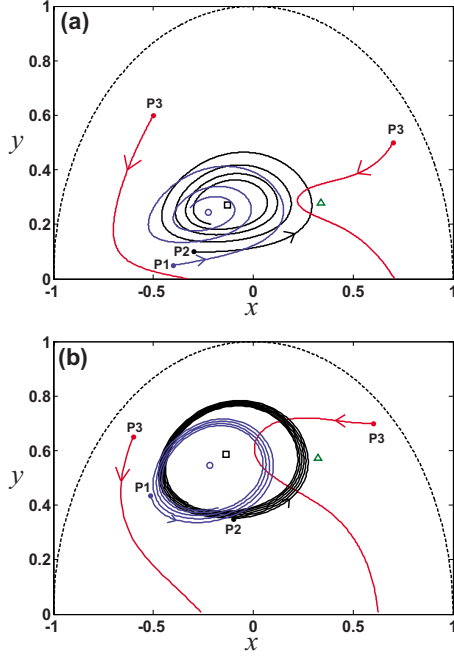


FIG. 11. (Color online) Particle sorting by size via point traps (indicated by open circles and squares) for Example 3: (a) no-slip vortex flow with $Ga=0.0105$ for P1; (b) free-slip vortex flow with $Ga=0.0633$ for P1. The point traps for the critical particle motion leading to complete separation are indicated by triangle symbols.

$=1:2:4$. In either no-slip or free-slip case, smaller particles P1 and P2 will be captured by their respective point traps (as indicated by an open circle and an open square), whereas the largest particles P3 will be pulled out of these traps onto the bottom surface by gravity. The critical particle radius for achieving complete separation is found to be $3.82R_1$ for the no-slip case and $3.88R_1$ for the free-slip case.

B. Particle sorting using limit cycle traps—Example 4

Here, we demonstrate particle sorting using limit cycle traps in two vortex flow structures set up by the following nonuniform slip velocity distributions:

$$u_{\text{slip}}(x) = 0.844(1 - x - x^2 + x^3) \quad \text{for no-slip flow,}$$

$$u_{\text{slip}}(x) = 0.844(1 + x - x^2 - x^3) \quad \text{for free-slip flow.}$$

The NDF force fields required to elicit a limit cycle are produced by a pair of source and sink points (essentially source and sink lines in the three-dimensional view). It is postulated that the particle is pushed by the repulsive force from the source point and at the same time is pulled by the attractive force from the sink point. We stipulate that the NDF force is acting along the direction from the particle toward the location of the source or sink point, and its magnitude is inversely proportional to their distance raised to the power n . Note that if n is equal to one, the force field will be divergence-free. To reflect the short-range and nondivergence-free nature, the respective force fields are given by the inverse power expressions with $n > 1$,

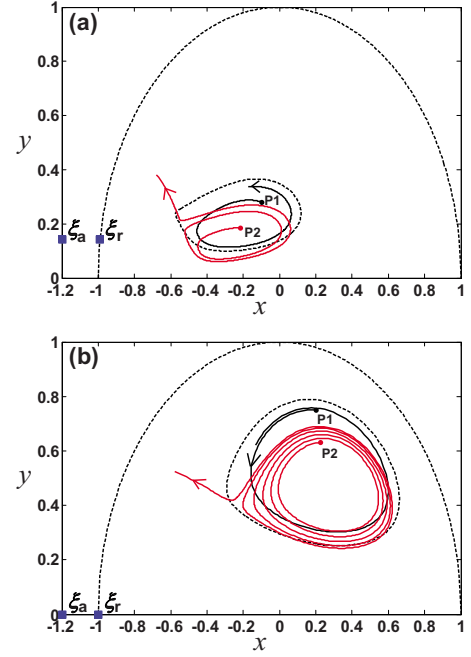


FIG. 12. (Color online) Particle sorting by mobility via limit cycle traps (pictured by the interior dotted lines) for Example 4: (a) no-slip vortex flow with $Z_{N1}\xi_r=0.166$; (b) free-slip vortex flow with $Z_{N1}\xi_r=3.97$. For particle P1 in the no-slip vortex flow, a supercritical Hopf bifurcation with $\alpha=-3.09$ would occur at $Z_{N1}\xi_r^*=0.211$ and $Z_{N1}\xi_a^*=0.529$, whereas for particle P1 in the free-slip vortex flow, a supercritical Hopf bifurcation with $\alpha=-0.0842$ would occur at $Z_{N1}\xi_r^*=4.22$ and $Z_{N1}\xi_a^*=6.15$.

$$E_{r,x} = \frac{x_p - x_r}{[(x_p - x_r)^2 + (y_p - y_r)^2]^{(1+n)/2}},$$

$$E_{r,y} = \frac{y_p - y_r}{[(x_p - x_r)^2 + (y_p - y_r)^2]^{(1+n)/2}},$$

$$E_{a,x} = \frac{-(x_p - x_a)}{[(x_p - x_a)^2 + (y_p - y_a)^2]^{(1+n)/2}},$$

$$E_{a,y} = \frac{-(y_p - y_a)}{[(x_p - x_a)^2 + (y_p - y_a)^2]^{(1+n)/2}}.$$

In the present analysis, we take $n=3$ for the no-slip vortex flow and $n=2$ for the free-slip vortex flow (the NDF force becomes shorter-range for the no-slip case). As marked in Figs. 12 and 13, the source point with the strength of ξ_r is placed at (x_r, y_r) to exert a repulsive force on the particles, whereas the sink point with the strength of ξ_a is placed at (x_a, y_a) to exert an attractive force on the particles. The design of the NDF force fields requires that the repulsive source point be closer to the particles in motion but the associated value of ξ_r be smaller. It is then possible that for a particular combination of ξ_r and ξ_a , particles of one identity will be trapped within a limit cycle, whereas those of another identity will leave out of the limit cycle trap according to the two phase portraits delineated in Fig. 9.

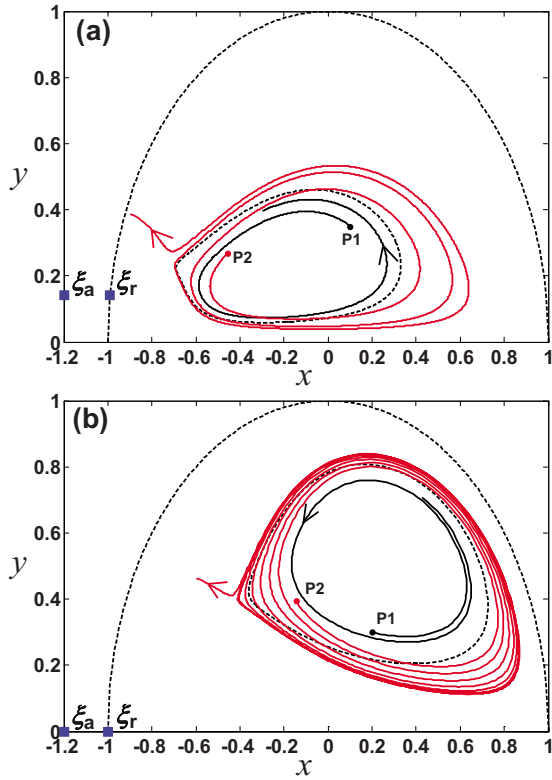


FIG. 13. (Color online) Particle sorting by size via limit cycle traps (pictured by the interior dotted lines) for Example 4: (a) no-slip vortex flow with $Ga=0.0084$ for particle P1; (b) free-slip vortex flow with $Ga=0.042$ for particle P1. For P1 in the no-slip vortex flow, a Hopf bifurcation with $\alpha=-0.357$ would occur at $Z_N\xi_r^*=0.211$ and $Z_N\xi_a^*=0.415$, whereas for P1 in the free-slip vortex flow, a Hopf bifurcation with $\alpha=-0.0941$ would occur at $Z_N\xi_r^*=4.22$ and $Z_N\xi_a^*=6.14$.

In the absence of DF forces, Fig. 12(a) uncovers the sorting scenario of two particles P1 and P2 with NDF mobilities $Z_{N1}:Z_{N2}=1:2$ in the no-slip vortex flow. Initially, the particles are aggregated by setting up a point trap near the vortex center. We then set $Z_{N1}\xi_r=0.166$ and $Z_{N1}\xi_a=Z_{N1}\xi_a^*$ to induce a stable limit cycle to trap particle P1, whose supercritical Hopf bifurcation with $\alpha=-3.09$ would occur at $Z_{N1}\xi_r^*=0.211$ and $Z_{N1}\xi_a^*=0.529$. For particle P2 with larger mobility Z_{N2} , the corresponding limit cycle goes beyond the stable manifold of the neighboring saddle point and is broken by the unstable manifold, as depicted in Fig. 9(b). So this particle will not fall into the limit cycle trap set up for particle P1 and go elsewhere, rendering a complete separation between the two particles, as shown in Fig. 12(a). Figure 12(b) shows similar particle separation using a limit cycle trap in the free-slip design with $Z_{N1}\xi_r=3.97$ and $Z_{N1}\xi_a=Z_{N1}\xi_a^*$.

A similar strategy can also be applied to sort particles of different sizes in vortex flows under gravity. Assume that two particles P1 and P2 have the same density and NDF mobility Z_N , but the radius of particle P2 is twice as large as particle P1. Namely, the gravity parameter Ga of particle P2 is four times that of particle P1. For particle P1, we can generate a limit cycle trap using the design values of $Ga=0.0084$, $Z_N\xi_r=0.160$, and $Z_N\xi_a=Z_N\xi_a^*$ for the no-slip case and

$Ga=0.042$, $Z_N\xi_r=3.91$, and $Z_N\xi_a=Z_N\xi_a^*$ for the free-slip case. The larger particle P2, subject to the greater gravitational pulling, is hard to maintain its own stable limit cycle. As a result, P1 can be readily captured by a limit cycle trap, whereas P2 is pulled out of the trap by gravity, as shown in Fig. 13. Both Figs. 12 and 13 suggest that it is possible to form multiple limit cycle traps for achieving localized separation of particles according to their multiple particle identities.

VI. CONCLUDING REMARKS

Motivated by particle manipulation with EOF in a microdroplet on an inhomogeneous substrate and by mimicking nonuniform boundary slip conditions in ICEO or ACEO, we have not only derived analytical solutions for the two-dimensional microvortex flow confined in a semicircular cap, but also studied the dynamics of particles in such a flow subject to various forces. We apply a linear stability analysis and develop a generic bifurcation theory to foresee the fates of suspended particles in the flow. More importantly, stable or unstable states can exist to offer excellent tools for achieving selective particle trapping, release, and sorting if the underlying flow and force fields are properly designed. These states are categorized as (i) a vortex trap around a stationary center, (ii) a point trap/release around a stable/unstable spiral point, and (iii) a ring trap along a stable limit cycle.

The key in realizing desired particle manipulation is to apply a nondivergence-free (NDF) force on a particle, turning a vortex center into a point trap/release or a limit cycle trap. If the NDF force is attractive, a broken vortex trap can release particles from an unstable spiral point, thus enhancing the subsequent particle trapping at a converging stagnation point. If a repulsive NDF force is used, a point trap (stable spiral point) can result to attract surrounding particles toward it. If both attractive and repulsive NDF forces work jointly to create a supercritical Hopf bifurcation, a limit cycle can form to trap particles into a ring. Either a point trap or a limit cycle trap furnishes the ability to capture particles at specific locations within the fluid. Therefore, these traps can be applied to selectively sort particles according to their properties.

In this work, we neglect inertial effects on particle dynamics because the Stokes number is very small in most microfluidic systems. Inertial effects, if non-negligible, would tend to drive the particles away from the vortex center, similar to the effects caused by an attractive NDF force. This is evident in Appendix D, showing that inertial effects always destabilize the center fixed point in a vortex flow.

Our study provides a useful framework to unravel particle dynamics in microvortices under the combined effects of advection and forces. It is interesting to note that the forces need not be externally applied. With inertia, it is possible to create a limit cycle trap by applying a repulsive NDF force or imposing a time-periodic perturbation upon the vortex flow. Results found in this study might offer new paradigms for achieving efficient particle manipulation and hence have potentials in realizing high-throughput screening in many on-chip applications.

ACKNOWLEDGMENTS

This work was supported by the National Science Council of Taiwan under Grants No. NSC 99-2221-E-006-202 of S.H.H. and No. NSC 97-2628-E-006-001-MY3 of H.H.W. H.C.C. was supported by DTRA under Grant No. CBDIF07-PRO013-2-0023.

APPENDIX A: DERIVATION OF FUNDAMENTAL SOLUTIONS

It is easy to see that Eqs. (5) and (6) satisfy $u_\theta=0$ and $u_r=0$ at $\theta=\pm\pi/2$, respectively, because $\sin(\pm m\pi/2)=0$ when m is even and $\cos(\pm m\pi/2)=0$ when m is odd. Equations (7a) and (7b) are constructed from the functions in Eqs. (6a) and (6b) to meet the additional condition of $u_\theta=0$ at $\theta=\pm\pi/2$. They can be rewritten as (assuming $\psi_0=0$).

$$\psi_3^{\text{odd}} = \sum_{m=1,3}^{\infty} c_m r^{m+2} [\sin m\theta + \sin(m+2)\theta], \quad (\text{A1a})$$

$$\psi_3^{\text{even}} = \sum_{m=0,2}^{\infty} c'_m r^{m+2} [\cos m\theta + \cos(m+2)\theta]. \quad (\text{A1b})$$

Note that in the above expansions, the functions $\sin m\theta + \sin(m+2)\theta$ (with odd m) and $\cos m\theta + \cos(m+2)\theta$ (with even m) satisfy $u_r=u_\theta=0$ at $\theta=\pm\pi/2$. Similarly, the functions in Eqs. (5a) and (5b) can be employed to yield another fundamental solution that also satisfies $u_r=u_\theta=0$ at $\theta=\pm\pi/2$, giving

$$\psi_6^{\text{odd}} = c_2 r^4 \sin 2\theta + \sum_{m=4,6}^{\infty} \left(\frac{m-2}{m} c_{m-2} r^m + c_m r^{m+2} \right) \sin m\theta, \quad (\text{A2a})$$

$$\psi_6^{\text{even}} = c'_1 r^3 \cos \theta + \sum_{m=3,5}^{\infty} \left(\frac{m-2}{m} c'_{m-2} r^m + c'_m r^{m+2} \right) \cos m\theta. \quad (\text{A2b})$$

Here, Eqs. (A1) and (A2) are combined in a subtle way to meet another homogeneous boundary condition, $\psi=0$ at $r=1$. We first select the coefficients $c_m (=d_{ik})$ and $c'_m (=d'_{ik})$, such that Eqs. (A1a) and (A1b) can be used to develop solutions that equal $\sin 2i\theta$ and $\cos(2i-1)\theta$ at $r=1$ ($i=1,2,\dots$), respectively. The coefficients d_{ik} and d'_{ik} can be calculated from

$$\sin 2i\theta = \sum_{j=1}^{\infty} \hat{d}_{ij} \sin(2j-1)\theta,$$

$$\cos(2i-1)\theta = \sum_{j=1}^{\infty} \hat{d}'_{ij} \cos(2j-2)\theta,$$

where

$$d_{ik} = \sum_{j=1}^k (-1)^{j+k} \hat{d}_{ij}, \quad d'_{ik} = \sum_{j=1}^k (-1)^{j+k} \hat{d}'_{ij}.$$

We then use Eqs. (A2a) and (A2b) to generate solutions that equal $-\sin 2i\theta$ and $-\cos(2i-1)\theta$ at $r=1$, respectively, giving

$$c_m = -\frac{m-2}{m} c_{m-2}, \quad c_{2i} = -1, \quad c_j = 0 \quad (j < 2i),$$

$$c'_m = -\frac{m-2}{m} c'_{m-2}, \quad c'_{2i-1} = -1, \quad c'_j = 0 \quad (j < 2i-1).$$

Adding up the derived two sets of solutions ensures $\psi=0$ at $r=1$ and leads to the fundamental solution presented in Eq. (8).

APPENDIX B: DERIVATION OF ANALYTICAL SOLUTION FOR CONFINED MICROVORTICES

The fundamental solution Eq. (5) that satisfies Eq. (10a) can also be made to satisfy Eq. (10b) by setting $b_m = -a_m$ and $b'_m = -a'_m$. The solution ψ_1 then reduces to ψ_5 as follows:

$$\psi_5^{\text{odd}} = \sum_{m=2,4}^{\infty} a_m (r^m - r^{m+2}) \sin m\theta, \quad (\text{B1a})$$

$$\psi_5^{\text{even}} = \sum_{m=1,3}^{\infty} a'_m (r^m - r^{m+2}) \cos m\theta. \quad (\text{B1b})$$

Comparing these equations with Eq. (11) for the slip velocity, the coefficients a_m and a'_m can be determined from the following formulas:

$$a_m = \frac{(-1)^{m/2}}{m} \sum_{\substack{j=1 \\ j=\text{odd}}}^{m-1} p_j, \quad m = 2, 4, \dots, \quad (\text{B2a})$$

$$a'_m = \frac{(-1)^{(m-1)/2}}{m} \sum_{\substack{j=0 \\ j=\text{even}}}^{m-1} p_j, \quad m = 1, 3, \dots. \quad (\text{B2b})$$

To satisfy the boundary condition at the cap, Eqs. (10c) or (10d), we make use of ψ_4 in Eq. (8) to derive the solution as follows. Recall that the functions ψ_{4i}^{odd} and ψ_{4i}^{even} in Eqs. (8c) and (8e) could be converted to represent u_θ or $\tau_{r\theta}$. The coefficients β_i and β'_i in Eqs. (8a) and (8b) are determined so as to cancel nonzero values of u_θ or $\tau_{r\theta}$ resulting from ψ_5 at $r=1$. Note that the functions of ψ_4 are not orthogonal with respect to the integration of θ from $-\pi/2$ to $\pi/2$. Therefore, the coefficients β_i or β'_i must be solved numerically by a set of algebraic equations with the number of truncation $N=10-20$ at best. The complete solution is thus obtained as $\psi = \psi_4 + \psi_5$.

If the no-slip condition of Eq. (10c) is used, β_i and β'_i are estimated from

$$\sum_{i=1}^N \beta_i \frac{\partial \psi_{4i}^{\text{odd}}}{\partial r} = -\frac{\partial \psi_5^{\text{odd}}}{\partial r} \quad \text{at } r=1, \quad (\text{B3a})$$

$$\sum_{i=1}^N \beta'_i \frac{\partial \psi_{4i}^{\text{even}}}{\partial r} = -\frac{\partial \psi_5^{\text{even}}}{\partial r} \quad \text{at } r=1. \quad (\text{B3b})$$

However, a subtle issue arises from the free-slip condition of Eq. (10d). As can be seen from Figs. 2(c) and 2(d), the shear stress $\tau_{r\theta}$ represented by the first set of the functions is identically zero at $r=1$. Obviously, this set of the functions cannot be used to adjust the value of the shear stress at the cap boundary. Hence, we omit the contribution from them and determine β_i and β'_i using

$$\begin{aligned} \sum_{i=2}^N \beta_i \left(\frac{\partial^2 \psi_{4i}^{\text{odd}}}{\partial \theta^2} + \frac{\partial \psi_{4i}^{\text{odd}}}{\partial r} - \frac{\partial^2 \psi_{4i}^{\text{odd}}}{\partial r^2} \right) \\ = - \left(\frac{\partial^2 \psi_5^{\text{odd}}}{\partial \theta^2} + \frac{\partial \psi_5^{\text{odd}}}{\partial r} - \frac{\partial^2 \psi_5^{\text{odd}}}{\partial r^2} \right) \quad \text{at } r=1, \end{aligned} \quad (\text{B4a})$$

$$\begin{aligned} \sum_{i=2}^N \beta'_i \left(\frac{\partial^2 \psi_{4i}^{\text{even}}}{\partial \theta^2} + \frac{\partial \psi_{4i}^{\text{even}}}{\partial r} - \frac{\partial^2 \psi_{4i}^{\text{even}}}{\partial r^2} \right) \\ = - \left(\frac{\partial^2 \psi_5^{\text{even}}}{\partial \theta^2} + \frac{\partial \psi_5^{\text{even}}}{\partial r} - \frac{\partial^2 \psi_5^{\text{even}}}{\partial r^2} \right) \quad \text{at } r=1. \end{aligned} \quad (\text{B4b})$$

Consequently, the solution obtained from Eq. (B4), $\psi^* = \psi_4(\beta_1 = \beta'_1 = 0) + \psi_5$, is incomplete because it does not satisfy $u_\theta = 0$ for the two corners at $\theta = \pm \pi/2$ and $r=1$. The first set of the functions are then employed to recover this zero corner condition, giving

$$\beta_1 = 0.3927 \left[\frac{\partial \psi^*}{\partial r}(1, -\pi/2) - \frac{\partial \psi^*}{\partial r}(1, \pi/2) \right], \quad (\text{B5a})$$

$$\beta'_1 = -0.7854 \left[\frac{\partial \psi^*}{\partial r}(1, -\pi/2) + \frac{\partial \psi^*}{\partial r}(1, \pi/2) \right]. \quad (\text{B5b})$$

APPENDIX C: OCCURRENCE OF A VORTEX TRAP IN THE ABSENCE OF NDF FORCE FIELDS

If the fixed point of Eq. (13) is a center, the similarity transformation can lead to a two-dimensional system of the form

$$\frac{d}{dt} \begin{pmatrix} x \\ y \end{pmatrix} = \begin{pmatrix} 0 & -\omega \\ \omega & 0 \end{pmatrix} \begin{pmatrix} x \\ y \end{pmatrix} + \begin{pmatrix} f(x,y) \\ g(x,y) \end{pmatrix} \quad (\text{C1})$$

with $f(0,0) = g(0,0) = 0$ and $\partial f^* / \partial x = \partial f^* / \partial y = \partial g^* / \partial x = \partial g^* / \partial y = 0$. This point corresponds to a Hopf bifurcation point in some occasions. The normal form theorem shows that by smooth changes of coordinates with the fixed point reduced to the origin, the above problem can be brought to the following form in polar coordinates [40],

$$\frac{dr}{dt} = \alpha r^3 + O(r^5), \quad (\text{C2a})$$

$$\frac{d\theta}{dt} = \omega + O(r^2). \quad (\text{C2b})$$

The normal form calculation could yield the first Lyapunov coefficient α as

$$\begin{aligned} \alpha = \frac{1}{16} \left[\left(\frac{\partial^2}{\partial x^2} + \frac{\partial^2}{\partial y^2} \right) \left(\frac{\partial f^*}{\partial x} + \frac{\partial g^*}{\partial y} \right) \right] \\ + \frac{1}{16\omega} \left[\left(\frac{\partial^2 f^*}{\partial y^2} \frac{\partial}{\partial y} - \frac{\partial^2 g^*}{\partial x^2} \frac{\partial}{\partial x} \right) \left(\frac{\partial f^*}{\partial x} + \frac{\partial g^*}{\partial y} \right) \right] \\ + \frac{\partial^2 f^*}{\partial x \partial y} \frac{\partial^2 f^*}{\partial x^2} - \frac{\partial^2 g^*}{\partial x \partial y} \frac{\partial^2 g^*}{\partial y^2}. \end{aligned}$$

It follows that if f and g constitute a DF field, then the first Lyapunov coefficient α is always zero. As a result, the particle trajectory tends to circulate around the fixed point and form a closed orbit. The statement is accurate at least to the order of r^5 . On the contrary, a NDF force may cause a Hopf bifurcation and a nonzero value of α .

APPENDIX D: EIGENVALUES OF A FIXED POINT IN THE PRESENCE OF SMALL INERTIAL EFFECT

In the presence of inertial, Eq. (13) should be expanded in dimension as

$$\frac{dx_p}{dt} = V_x(t), \quad (\text{D1a})$$

$$\frac{dy_p}{dt} = V_y(t), \quad (\text{D1b})$$

$$\text{St} \frac{dV_x}{dt} = -V_x(t) + F[x_p(t), y_p(t)], \quad (\text{D1c})$$

$$\text{St} \frac{dV_y}{dt} = -V_y(t) + G[x_p(t), y_p(t)]. \quad (\text{D1d})$$

For the small inertial effect with $\text{St} = \varepsilon \ll 1$, the Jacobian matrix at the fixed point $(\bar{x}_p, \bar{y}_p, \bar{V}_x, \bar{V}_y)$ in Eq. (D1) can be expressed as

$$\mathbf{J}_\varepsilon(\bar{x}_p, \bar{y}_p, \bar{V}_x, \bar{V}_y) = \frac{1}{\varepsilon} \begin{bmatrix} 0 & 0 & \varepsilon & 0 \\ 0 & 0 & 0 & \varepsilon \\ \frac{\partial F^*}{\partial x_p} & \frac{\partial F^*}{\partial y_p} & -1 & 0 \\ \frac{\partial G^*}{\partial x_p} & \frac{\partial G^*}{\partial y_p} & 0 & -1 \end{bmatrix}. \quad (\text{D2})$$

The four eigenvalues with inertia λ_ε of \mathbf{J}_ε can be related to those without inertia λ_\pm [c.f. Eq. (15a)] as $\lambda_\varepsilon(1+\varepsilon\lambda_\varepsilon)=\lambda_\pm=\sigma\pm j\omega$. The two eigenvalues associated with (x_p, y_p) can then be approximated by

$$\lambda_\varepsilon \approx \varepsilon(\omega^2 - \sigma^2) + \sigma \pm j\omega(1 - 2\sigma\varepsilon), \quad (\text{D3})$$

whose real part is greater than zero as the fixed point is at the vortex center with $\sigma=0$. This implies that inertial effects

always destabilize the center fixed point. Similarly, those associated with (V_x, V_y) are

$$\lambda_\varepsilon \approx -1/\varepsilon - \sigma - \varepsilon(\omega^2 - \sigma^2) \mp j\omega(1 - 2\sigma\varepsilon), \quad (\text{D4})$$

whose real part approaches $-\infty$ for a vanishing ε , implying that the particle velocity will quickly reach its steady state.

-
- [1] A. W. Martinez, S. T. Phillips, B. J. Wiley, M. Gupta, and G. M. Whitesides, *Lab Chip* **8**, 2146 (2008).
- [2] J. Wu, Y. Ben, D. Battigelli, and H. C. Chang, *Ind. Eng. Chem. Res.* **44**, 2815 (2005).
- [3] L. Y. Yeo and J. R. Friend, *Biomicrofluidics* **3**, 012002 (2009).
- [4] H. C. Chang and G. Yossifon, *Biomicrofluidics* **3**, 012001 (2009).
- [5] D. Hou, S. Maheshwari, and H. C. Chang, *Biomicrofluidics* **1**, 014106 (2007).
- [6] L. Y. Yeo, D. Hou, S. Maheshwari, and H. C. Chang, *Appl. Phys. Lett.* **88**, 233512 (2006).
- [7] S. K. Thamida and H. C. Chang, *Phys. Fluids* **14**, 4315 (2002).
- [8] Y. Ben and H. C. Chang, *J. Fluid Mech.* **461**, 229 (2002).
- [9] S. Qian and H. H. Bau, *Anal. Chem.* **74**, 3616 (2002).
- [10] T. M. Squires and M. Z. Bazant, *J. Fluid Mech.* **509**, 217 (2004).
- [11] E. Brunet and A. Ajdari, *Phys. Rev. E* **73**, 056306 (2006).
- [12] A. Ramos, H. Morgan, N. G. Green, and A. Castellanos, *J. Colloid Interface Sci.* **217**, 420 (1999).
- [13] A. Ajdari, *Phys. Rev. E* **61**, R45 (2000).
- [14] A. González, A. Ramos, N. G. Green, A. Castellanos, and H. Morgan, *Phys. Rev. E* **61**, 4019 (2000).
- [15] D. Holmes and H. Morgan, *Particle Focusing and Separation Using Dielectrophoresis in a Microfluidic Device* (Kluwer Academic Publishers, Massachusetts, 2001).
- [16] P. K. Wong, T. H. Wang, J. H. Deval, and C. M. Ho, *IEEE/ASME Trans. Mechatron.* **9**, 366 (2004).
- [17] J. Kreft, Y. L. Chen and H. C. Chang, *Phys. Rev. E* **77**, 030801(R) (2008).
- [18] J. R. Du, Y. J. Juang, J. T. Wu, and H. H. Wei, *Biomicrofluidics* **2**, 044103 (2008).
- [19] D. Hou and H. C. Chang, *Phys. Fluids* **18**, 071702 (2006).
- [20] M. R. Maxey and J. J. Riley, *Phys. Fluids* **26**, 883 (1983).
- [21] J. Rubin, C. K. R. T. Jones, and M. Maxey, *J. Nonlinear Sci.* **5**, 337 (1995).
- [22] O. A. Druzhinin, L. A. Ostrovsky, and Yu. A. Stepanyants, *Chaos* **3**, 359 (1993).
- [23] J. R. Angilella, *Phys. Fluids* **19**, 073302 (2007).
- [24] K. K. Tio, A. M. Ganan-Calvo, and J. C. Lasheras, *Phys. Fluids A* **5**, 1679 (1993).
- [25] B. Marcu, E. Meiburg, and P. K. Newton, *Phys. Fluids* **7**, 400 (1995).
- [26] R. D. Vilela and A. E. Motter, *Phys. Rev. Lett.* **99**, 264101 (2007).
- [27] T. Sapsis and G. Haller, *Chaos* **20**, 017515 (2010).
- [28] J. R. Angilella, e-print [arXiv:1003.3842](https://arxiv.org/abs/1003.3842).
- [29] T. Nizkaya, J. R. Angilella, and M. Bues, e-print [arXiv:1003.4644](https://arxiv.org/abs/1003.4644).
- [30] S. J. Liu, S. H. Hwang, and H. H. Wei, *Langmuir* **24**, 13776 (2008).
- [31] H. H. Wei, *J. Colloid Interface Sci.* **284**, 742 (2005).
- [32] D. Halpern and H. H. Wei, *Langmuir* **23**, 9505 (2007).
- [33] S. J. Kim, K. H. Kang, J. G. Lee, I. S. Kang, and B. J. Yoon, *Anal. Chem.* **78**, 5192 (2006).
- [34] L. G. Leal, *Laminar Flow and Convective Transport Processes: Scaling Principles and Asymptotic Analysis* (Butterworth-Heinemann College, Boston, 1992).
- [35] A. Babiano, J. H. E. Cartwright, O. Piro, and A. Provenzale, *Phys. Rev. Lett.* **84**, 5764 (2000).
- [36] H. Stommel, *J. Mar. Res.* **8**, 24 (1949).
- [37] Z. Gagnon and H. C. Chang, *Electrophoresis* **26**, 3725 (2005).
- [38] R. J. Hunter, *Foundation of Colloid Science*, 2nd ed. (Oxford University Press, New York, 2001).
- [39] R. F. Probstein, *Physicochemical Hydrodynamics*, 2nd ed. (Wiley, New York, 1994).
- [40] J. Guckenheimer and P. Holmes, *Nonlinear Oscillations, Dynamical Systems, and Bifurcations of Vector Fields* (Springer-Verlag, New York, 1983).